



Ruan, S., Yang, E.-H. and Unluer, C. (2021) Production of reactive magnesia from desalination reject brine and its use as a binder. *Journal of CO2 Utilization*, 44, 101383. (doi: [10.1016/j.jcou.2020.101383](https://doi.org/10.1016/j.jcou.2020.101383)).

This is the author's final accepted version.

There may be differences between this version and the published version. You are advised to consult the publisher's version if you wish to cite from it.

<http://eprints.gla.ac.uk/232313/>

Deposited on: 17 February 2021

Enlighten – Research publications by members of the University of Glasgow
<http://eprints.gla.ac.uk>

34 1. Introduction

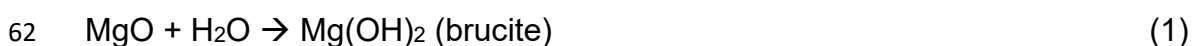
35

36 Reactive magnesia (MgO) can be obtained from the calcination of magnesite
37 (MgCO₃) at a temperature of 800-1000°C (i.e. dry route) [1, 2], magnesium
38 silicates (e.g. serpentine) [3] or extracted from seawater or brine (i.e. wet route)
39 [4]. While the majority of MgO production is currently through the processing of
40 naturally occurring minerals such as magnesite, around 14% of MgO is
41 synthesized via the calcination of Mg-bearing phases, which are precipitated
42 from seawater or brine sources that contain high concentrations of Mg²⁺ [5]. The
43 extraction of MgO through the wet route involves the use of an alkali base that
44 enables the precipitation of Mg-bearing products such as magnesium hydroxide
45 and magnesium oxalate in the first stage. The obtained precipitates are then
46 separated, washed and heated to produce MgO at a low calcination
47 temperature [4, 6-10].

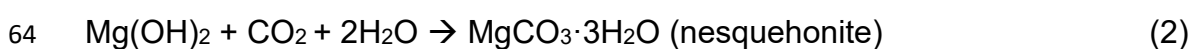
48

49 Synthetic MgO obtained from seawater/brine via the wet route usually
50 demonstrates a higher purity, reactivity and specific surface area (SSA) in
51 comparison to MgO obtained from the calcination of magnesite via the dry route
52 [11]. Due to these advantages, the chemically synthesized MgO finds uses in
53 high-end applications in pharmaceutical, semiconductor and refractory
54 industries, where it can be used as an additive or a catalyst [5, 12]. Another
55 increasingly popular use of MgO is as a cementitious binder [5, 13-27] or an
56 expansive additive [13, 28] in concrete formulations. Relying on its ability to
57 gain strength via carbonation [14, 29-34], reactive MgO cement-based concrete
58 samples have revealed significant strength gains, meanwhile enabling the long-
59 term sequestration of CO₂ in the form of stable carbonates, as shown in
60 Equations 1-4.

61



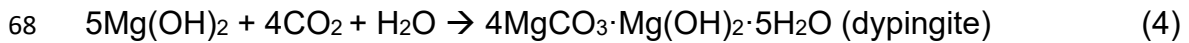
63



65



67



69

70 A large number of magnesite deposits are mainly located in China and North
71 Korea, which limits global access to this raw material [5]. While the production
72 of MgO via the dry route and its use as a binder has been investigated in terms
73 of its environmental impacts [35, 36] and performance in comparison to PC [2,
74 37], the shortage of magnesite and CO₂ emissions associated with the dry route
75 led to an increase in interest towards chemically synthesized MgO. Alternatively,
76 the production of MgO from the wet route presents several advantages in terms
77 of the abundance of resources (e.g. seawater, brines etc.) and production of
78 MgO with a high purity and reactivity. The relatively higher energy consumption
79 of this production route (i.e. 17 vs. 5.9 GJ per tonne of MgO [38]) is the largest
80 drawback in its large-scale adaptation. However, this energy demand can be
81 reduced when reject brine is used as the main raw material [4]. Further
82 improvements in the production process and implementation of cleaner
83 production methods that increase the utilization rate of resources and reduce
84 CO₂ emissions can promote the sustainability of MgO production [39, 40] and
85 result in economic gains [41].

86

87 Desalination is regarded as an important alternative approach to satisfy the
88 increasing residential and industrial water demands in water-stressed countries
89 such as Singapore [42]. Current global brine production by ~16,000
90 desalination plants worldwide stands at 141.5 million m³/day, totaling 51.7
91 billion m³/year [43]. Assuming a MgCl₂ content of 122 g/L in brine [5], this
92 corresponds to a yearly MgO production of around 2659 million tonnes. This
93 amount is expected to increase with the increasing demand on the use of
94 desalination plants on a global level. Similarly, three desalination plants in
95 Singapore provide 130 million gallons of drinking water per day. With two
96 additional desalination plants being built (i.e. Marina East and Jurong Island
97 desalination plants), the five desalination plants will provide a total of ~190
98 million gallons of water per day by 2020 [44]. The production of desalination
99 water generates an equivalent amount of reject brine, a concentrated by-
100 product produced at the end of the desalination process [45, 46]. Reject brine
101 is often discharged directly back into the sea, which threatens marine life and

102 ecosystem because of its high salinity and increased temperatures [47].
103 Therefore, the disposal and management of reject brine is considered as a
104 major challenge as well as an environmental threat [46, 48].

105

106 Reject brine has a great potential to be used as a sustainable source for cement
107 production due to its high magnesium (Mg^{2+}) content (i.e. 30% more than
108 seawater) and abundance on both local and global levels. Although a number
109 of studies [6, 7, 49-52] reported the synthesis of MgO or its derivatives from
110 seawater, natural brine or synthetic solutions; the use of reject brine presents
111 a different scenario in terms of its chemical composition. Accordingly, reject
112 brine contains high concentrations of different dissolved salts and suspended
113 constituents incorporated during the desalination process, which involves the
114 use of various chemicals to enable the precipitation of colloidal particles before
115 the filtration process [53].

116

117 Several studies [9, 10, 47, 49, 54-56] suggested the use of alkali sources such
118 as sodium carbonate (Na_2CO_3), ammonium hydroxide (NH_4OH) and sodium
119 hydroxide ($NaOH$) to enable the precipitation of Mg-bearing phases from
120 seawater/brine. The efficiency of the synthesis was determined by the type and
121 amount of the alkali base introduced into the reject brine, during which strong
122 bases were favored in the precipitation of brucite from the seawater or brine [9,
123 49]. Accordingly, a recovery rate of 97-99% for magnesium was achieved via
124 the use of $NaOH$ ($pH > 11$) [57, 58]. $NaOH$ was also used with oxalic acid
125 ($C_2H_2O_4$), facilitating the precipitation of magnesium oxalate (MgC_2O_4) from
126 brine, which was then heated to obtain MgO with a high purity and reactivity [9].
127 The characteristics of intermediate phases (e.g. $Mg(OH)_2$) and the final product,
128 MgO, significantly varied with the introduction of different alkali bases,
129 especially in terms of reactivity, purity and other key chemical and physical
130 aspects controlling the performance of MgO as a cementitious binder [47, 49].

131

132 Reactive MgO cement has several advantages when compared to Portland
133 cement (PC), including its ability to gain high strengths by absorbing and storing
134 atmospheric CO_2 permanently in the form of stable carbonates and its
135 recyclability at the end of its lifetime [14, 34, 59-64]. In line with these

136 advantages, the main objective of this study is to develop reactive MgO from
137 locally available reject brine and evaluate its feasibility to be used as a binder
138 in terms of mechanical performance and microstructural development, which
139 has not been reported until now. Although reactive MgO synthesized from reject
140 brine is known to have a higher reactivity and SSA compared with other
141 commercial sources of MgO produced through the dry route, its incorporation
142 into cement-based mixes has not been performed before, possibly due to its
143 relatively low yield in a small laboratory setup [4, 9]. Therefore, this study also
144 addressed the key aspects of scaling up the production of MgO from reject brine,
145 which was then used in the preparation of cement-based mixes and their
146 subsequent analyses.

147

148 The work presented in this study followed 5 main stages: (i) synthesis of MgO
149 from reject brine obtained from a local desalination plant, (ii) characterization of
150 the synthesized MgO and its comparison to a commercial product, (iii)
151 measurement of mechanical properties, (iv) evaluation of phase formations and
152 microstructural development and (v) assessment of environmental impacts.
153 During the initial stage, MgO synthesized from reject brine was characterized
154 and compared to a commercial MgO (i.e. produced via the dry route) by acid
155 reactivity test. This was followed by the use of these 2 MgO powders (i.e. one
156 synthesized from reject brine in the lab and the other provided by a commercial
157 source for comparison purposes) as the main binder in the preparation of
158 mortar samples, which were cured under a CO₂ concentration of 10% for up to
159 28 days.

160

161 The mechanical performance of the prepared samples was assessed via the
162 measurement of compressive strength. To obtain the extent of hydration and
163 carbonation and to evaluate the microstructural development of each sample,
164 x-ray diffraction (XRD), thermogravimetric analysis (TGA) / differential scanning
165 calorimetry (DSC) and field emission scanning electron microscopy (FESEM)
166 were used. In the final stage, the IPCC 2007 method, based on the Fourth
167 Assessment Report of the Intergovernmental Panel on Climate Change (IPCC),
168 was used to obtain the carbon footprint of the production of MgO through the
169 wet route and its use as a binder to indicate its feasibility from an environmental

170 standpoint.

171

172

173 **2. Materials and Methodology**

174

175 **2.1 Materials**

176

177 The raw material used in the production of MgO, reject brine, was obtained from
178 a local seawater desalination plant, which adopts a reverse osmosis (RO)
179 membrane system to purify saline water and produce drinkable water. These
180 membranes reject more than 99.5% of the dissolved salts and the suspended
181 materials in the feedwater, resulting in a highly concentrated reject waste
182 stream. This waste contains a large number of suspended constituents and a
183 2-7 fold increased concentration of dissolved salts [42]. Prior to analysis, the
184 suspended particles were removed by an injector filter (45 μm), revealing a pH
185 of 8 for the reject brine. ICP-OES (PerkinElmer Optima DV2000) was used to
186 analyze the chemical composition of the reject brine, which is shown in Table
187 1. The concentration of Mg^{2+} was measured as 1603 PPM, along with other
188 elements such as Na^+ , K^+ and Ca^{2+} . To enable the precipitation of $\text{Mg}(\text{OH})_2$ in
189 the reject brine solution, the alkali base used was sodium hydroxide (NaOH,
190 reagent grade, pellets), obtained from VWR Pte Ltd (Singapore).

191

192 A commercial reactive MgO, produced via the calcination of magnesite (dry
193 route) and provided by International Scientific Ltd (Singapore), was also used
194 for comparison purposes. The chemical composition of this commercial reactive
195 MgO, provided by the supplier, is presented in Table 2. Natural sand (0-4 mm,
196 median particle diameter (D_{50}) = 0.7 mm, coefficient of uniformity (C_U) = 3.6),
197 obtained from Buildmate Pte Ltd (Singapore), was also used as fine aggregates
198 in the prepared mortar samples.

199

200

201 **2.2 Sample preparation**

202

2.2.1 Production of MgO from reject brine

2.2.1.1 Production of MgO on a small scale

The first step involved in the synthesis of MgO from reject brine was the addition of NaOH solution to the brine in a beaker, at a NaOH/Mg²⁺ molar ratio of 2, which was determined in line with the findings of previous studies [9, 47]. The solution was mixed by a magnetic stirrer at a speed of 300 RPM under room temperature (i.e. 25°C). A pH/thermometer probe was used to continuously monitor the reaction degrees. The reaction was completed when the pH of the system stabilized. The separation of the newly-formed precipitates and liquid was conducted via a centrifuge, followed by the washing of the solid phases three times with ultra-pure water to remove any surface-attached ions. The solid-liquid separation was also repeated for three times. The washed solids were placed in an oven at 105°C for 1 day to enable the removal of the free water. Afterwards, they were then ground into powder form to pass through a 125 µm sieve, followed by calcination in an electric furnace at a temperature of 500°C for 2 hours to convert Mg(OH)₂ into MgO (particle size: D₁₀ = 4.9 µm; D₅₀ = 30.5 µm; D₉₀ = 71.4 µm), in line with the findings of a previous study [9]. While straightforward, this lab-scale setup led to the precipitation of only ~2 grams of Mg(OH)₂ from 1 L of reject brine.

2.2.1.2 Production of MgO on a large scale

The limited MgO output obtained in the lab-scale setup (i.e. 2 grams MgO per L of reject brine), highlighted the need to scale up the production of MgO to produce a sufficient amount for the preparation and analysis of cement-based samples (e.g. mortar). To enable this, a larger reaction tank with a volume of 20 L, resulting in a higher MgO yield of 40 grams for every batch, was adopted instead of a 1 L beaker used previously. Considering the Mg concentration in the reject brine (i.e. ~8%) and the density of reject brine (1200 kg/m³), the actual yield was lower than the theoretical one. The following procedure was followed to scale up the production of MgO:

237

238 (i) The NaOH solution was added into the 20 L reaction tank at a NaOH/Mg²⁺
239 molar ratio of 2, during which the pH was recorded continuously.

240

241 (ii) Due to the large size of the reaction tank, the solution was shaken manually
242 (i.e. for 5 minutes every hour) instead of using a magnetic stirrer. The pH of the
243 solution was measured until it reached a stable value, indicating the completion
244 of the reaction.

245

246 (iii) After 24 hours of natural separation, the solid precipitates, which naturally
247 accumulated at the bottom of the tank, were separated from the solution by
248 pouring out the liquid.

249

250 (iv) The separation, drying and calcination of the precipitates were performed
251 as mentioned in Section 2.2.1.1.

252

253 Fig. 1 presents the microstructural images of MgO obtained from the reject
254 brine via the calcination of the precipitated Mg(OH)₂ at a temperature of 500°C
255 for 2 hours. The figure revealed the porous structures of both powders and the
256 more pronounced roughness of the surface of synthetic MgO than commercial
257 MgO, which could be related to its lower crystallinity and higher reactivity. The
258 XRD patterns of the synthesized and commercial MgO are shown in Fig. 2. As
259 can be seen from these patterns, CaCO₃ was the major impurity in synthetic
260 MgO sample, whereas other impurities such as magnesite and brucite were
261 found in commercial MgO. The presence of these impurities was associated
262 with the incomplete decomposition of the raw material (i.e. magnesite) and the
263 partial hydration of MgO during storage. The particle size distribution (PSD) of
264 synthetic and commercial MgO powders is shown in Fig. 3, indicating the
265 smaller particle size of the synthetic MgO than the commercial MgO.

266

267

268 **2.2.2 Preparation of mortar samples**

269

270 Two sets of mortar samples, one incorporating the MgO synthesized from reject

271 brine (Syn-M), the other using the commercial MgO (Com-M), were prepared
272 in line with the mix designs shown in Table 3. The sand-to-binder (s/b) ratios of
273 both sets of samples were kept constant at 1. The water-to-binder (w/b) ratios
274 were determined as 0.83 and 0.53 to produce Syn-M and Com-M samples with
275 similar workabilities, respectively. The higher water demand of synthetic MgO
276 was in line with its smaller particle size (Fig. 3), which required larger amounts
277 of water to reach the same consistency as commercial MgO. In terms of Com-
278 M, previous studies [16] indicated that a w/b ratio of 0.55-0.6 revealed the best
279 performance within these samples. Considering that the theoretical water/MgO
280 ratio needed according to the chemical formula corresponding to the hydration
281 of MgO is 0.45, the slightly higher w/b ratio used in the preparation of samples,
282 which took into account other factors such as the agglomeration of MgO
283 particles and potential evaporation during sample preparation, was sufficient to
284 reflect the potential of Com-M samples in practice [65].

285

286 To prepare the mortar mixtures, the dry ingredients were mixed first in a bench
287 scale mixer, followed by the gradual addition of water. Mixing continued until a
288 homogenous mixture was obtained. The prepared mixture was then cast into
289 20×20×20 mm³ cubic molds, consolidated by a vibrating table and trowel
290 finished. All samples were demolded after 1 day and were cured under
291 carbonation conditions (28±2°C, 80±5% RH, 10% CO₂) for up to 28 days.

292

293 Fig. 4 shows a summary of the procedure followed during this process, starting
294 from the acquirement of the reject brine from a reverse osmosis desalination
295 plant in Singapore [66], to the synthesis and use of MgO in the preparation and
296 analysis of mortar samples.

297

298

299 **2.3 Methodology**

300

301 **2.3.1 Reactivity**

302

303 The reactivities of both sources of MgO were measured by an acid
304 neutralization test. To initiate the analysis, 0.28 g of synthetic MgO was added

305 into 50 ml of citric acid solution (i.e. concentration of 0.07 mol/l). The time taken
306 for the neutralization of the acid solution was reported as an indication of
307 reactivity [5, 11, 13].

308

309

310 **2.3.2 Compressive strength**

311

312 The compressive strengths of the prepared samples were measured at 3, 7 and
313 28 days by uni-axial loading in triplicates, in line with ASTM C109/C109M-16a
314 [67]. The equipment used was a universal testing machine (INSTRON 5900R)
315 operated under a displacement control mode at 0.5 mm/min.

316

317

318 **2.3.3 Microstructural analyses**

319

320 Samples extracted from the cubes crushed during the strength testing were
321 stored in acetone for 3 days to stop hydration, followed by vacuum drying for 3
322 days, prior to x-ray diffraction (XRD), thermogravimetric analysis / differential
323 scanning calorimetry (TGA/DSC) and field emission scanning electron
324 microscopy (FESEM) analyses. The dried samples were ground down to pass
325 through a 125 μm sieve before they were analysed under XRD and TGA/DSC.
326 The results of these analyses depend on the location of the selected sample as
327 the intensities of carbonates peaks (i.e. indicating the contents of carbonate
328 phases) reduce as the sample depth increases due to the inhibited diffusion of
329 CO_2 at greater sample depths [68]. Therefore, to avoid any inconsistencies in
330 the final results due to the sample depth, the powders used in all the
331 microstructural analyses were all derived from the surfaces of the crushed
332 samples.

333

334 XRD data was recorded on a Philips PW 1800 spectrometer by using Cu K α
335 radiation (40 kV, 40 mA), with a scanning rate of 2° 2 θ /step, from 5° to 80° 2 θ .
336 Quantification of all major phases was performed via the Rietveld refinement
337 software TOPAS 5.0, with a fundamental parameter approach [69]. TGA/DSC
338 was conducted on a Perkin Elmer TGA 4000 equipment, operated from 40°C

339 to 900°C, at a heating rate of 10°C/min, under a nitrogen flow. For the
340 investigation of the morphologies of reaction phases, the dried samples were
341 mounted onto aluminium stubs using double-sided adhesive carbon disks and
342 sputter-coated with gold prior to their analysis via a JOEL JSM-7600F FESEM.

343

344

345 **2.3.4 CO₂ emissions**

346

347 The environmental impacts of the production and use of MgO via the wet route
348 were assessed via the calculation of CO₂ emissions associated with these
349 processes. The functional unit used for this purpose was 1 kg MgO, analyzed
350 via IPCC 2007 approach with a timeframe of 100 years [70]. Considering its
351 waste nature, the inputs and outputs due to the acquirement of reject brine were
352 supposed to be zero. The inventory for the alkali source (NaOH) was obtained
353 from the ETH-ESU database, provided by Eidgenössische Technische
354 Hochschule [71]. To produce 1 kg of MgO, 1.45 kg of Mg(OH)₂ was precipitated,
355 requiring 2 kg of NaOH and generating 0.45 kg of water.

356

357 Since there was no inventory on the energy required for the calcination of
358 brucite at 500°C, the environmental impacts associated with this step were
359 obtained from theoretical calculations, for which the individual heat capacity and
360 enthalpy of each material were obtained from [72]. The details of these
361 calculations are included in the Appendix. Accordingly, for the production of 1
362 kg of MgO, 0.687 kWh of electricity was used during the calcination of brucite
363 at 500°C. Considering 95% of Singapore's electricity is produced using natural
364 gas [73], this was taken into account in the calculation. Furthermore, a
365 sensitivity analysis was performed to take into account various energy sources
366 including coal (i.e. the most widely used energy source in some developing
367 countries such as China) and nuclear power (i.e. more common in some
368 European countries). The carbon footprint of synthetic MgO was also compared
369 with that of commercial MgO produced via the calcination of magnesite, whose
370 details were reported in a previous study [1].

371

372

373 **3. Results and Discussion**

374

375 **3.1 Reactivity**

376

377 The reactivities of Syn-M (i.e. produced on small and large scales) and Com-
378 M, measured via the time it took for the neutralization of citric acid, are shown
379 in Fig. 5. Syn-M samples, produced on small and large scales, revealed
380 comparable reactivities. These results indicated that the scaling up of MgO
381 production to the level presented in this study would not compromise the
382 reactivity of the final product, meanwhile resulting in a much higher yield of MgO.
383 The reactivity of synthetic MgO could be further improved via the optimization
384 of the calcination temperature and the residence time, enabling the complete
385 decomposition of brucite ($\text{Mg}(\text{OH})_2$) and a higher reactivity of MgO.

386

387 In line with the findings of previous studies [11], synthetic MgO revealed a
388 greater reactivity when compared to commercial MgO obtained from the
389 calcination of magnesite. The improved reactivity of synthetic MgO could be
390 due to its smaller particle size (i.e. higher specific surface area), higher purity
391 and lower crystallinity, indicating higher structural defects on its surface. The
392 influence of other key factors, such as the alkali source, on the properties of the
393 final product, also need to be considered. Accordingly, the use of NH_4OH was
394 reported to generate MgO samples with porous structures, which led to higher
395 SSA and reactivity than MgO that was synthesized via the use of NaOH under
396 the same calcination conditions [74]. Another factor that is important in the
397 determination of SSA during the manufacturing of MgO is grinding. In practice,
398 different mills can be used to reduce the particle size of MgO, which has a fine
399 nature due to the precipitation process [5]. To reduce the size further, the
400 powders could undergo milling, involving the use of ball mills or ring roller mills.
401 Finally, increases in the calcination temperature and time lead to a reduction in
402 the SSA and an increase in the crystallinity of MgO, along with the
403 agglomeration of particles, thereby reducing its reactivity [5, 74, 75]. Therefore,
404 the smaller particle size and higher SSA of synthetic MgO than commercial
405 MgO were associated with the differences in the parent materials (i.e. reject
406 brine/brucite vs. magnesite), manufacturing route (i.e. wet vs. dry) and

407 calcination temperatures (i.e. 500°C vs. ~800°C).

408

409 The calcination of brucite (i.e. precursor of synthetic MgO) at a lower
410 temperature (500°C) than the calcination temperature (~800°C) used during the
411 production of commercial MgO from magnesite was associated with the
412 difference in the temperatures required for the complete decomposition of
413 brucite and magnesite. Accordingly, the higher calcination temperature used in
414 the decomposition of magnesite led to a final product (i.e. commercial MgO)
415 with a smaller specific surface area, increased crystallinity and therefore, lower
416 reactivity than its synthetic counterpart [5]. Similarly, the differences in parent
417 materials and production routes led to different purity levels. Amongst these two
418 MgO samples, the quarrying and incomplete decomposition of magnesite
419 involved higher impurities than the chemical synthesis of MgO from reject brine.
420 Alternatively, the presence of calcite in synthetic MgO could be attributed to the
421 reaction between Ca^{2+} and CO_2 during the synthesis.

422

423 It must also be noted that the large-scale commercial production of MgO in
424 practice involves the acceleration of the decomposition of magnesite by using
425 higher calcination temperatures than 800°C to achieve a high production rate.
426 The maintenance of these high temperatures until the discharge of CO_2 is
427 completed further reduces the reactivity of commercial MgO obtained from the
428 calcination of magnesite [5]. On the other hand, the comparable reactivities of
429 synthetic MgO samples produced on small and large scales were an indication
430 of the feasibility of the large-scale production of MgO without significantly
431 changing its final properties. Therefore, this route was chosen for the production
432 of MgO used in the subsequent analyses in this study. It should be noted that,
433 as this study demonstrated a small-scale production of MgO from reject brine,
434 the degree of grinding was not precisely controlled as it would be on a large-
435 scale production plant. This is an important parameter as it would influence the
436 final particle size distribution of the synthetic MgO and associated properties
437 when produced on a large-scale.

438

439

3.2 Compressive strength

The compressive strengths of Syn-M and Com-M samples cured for up to 28 days are shown in Fig. 6. Both samples revealed a steady increase in strength over time, which was associated with the continuation of the hydration and carbonation processes. Amongst the two samples, Syn-M revealed higher strengths than Com-M samples at all durations, resulting in ~62% higher strengths at 28 days. This difference in strength was in line with the higher reactivity of Syn-M (Fig. 5). As the reaction rate of MgO is greatly determined by its reactivity [76], the higher reactivities of Syn-M samples could have enhanced the hydration and carbonation processes within these samples, possibly leading to the formation of a larger amount of hydration and carbonation phases (Equations 1-4).

Another factor that played a key role in the strength results was the different w/b ratios of the two binders, which were adjusted according to their standard consistencies. While water can provide a medium for the occurrence of hydration and carbonation reactions and enable increased diffusion of CO₂ via the provision of a larger capillary porosity; it can also hinder the rate of CO₂ diffusion due to the saturated nature of the pores and lower the overall performance via the higher porosity [16, 34, 60]. Although Syn-M samples outperformed Com-M samples at all durations, a further adjustment of the w/b ratio that would enable the reduction of the water content could lead to even higher strengths.

3.3 XRD

The XRD patterns of Syn-M and Com-M samples after 7 days of curing are shown in Fig. 7. The major hydrated magnesium carbonate (HMC) detected in the XRD patterns of both samples was hydromagnesite ($\text{Mg}_5(\text{CO}_3)_4(\text{OH})_2 \cdot 4\text{H}_2\text{O}$; PDF #025-0513), with highest intensity peaks located at 13.7°, 15.3° and 30.8° 2θ. In addition to hydromagnesite, the presence of un-hydrated MgO and un-carbonated brucite was also observed in both samples, indicating the

474 incomplete hydration and carbonation reactions, respectively. Quartz peaks
475 were also present due to the use of sand in sample preparation.

476

477 Table 4 shows the contents of major phases within both samples after 7 days
478 of curing. When compared with previous studies [16, 17, 60, 77], the total
479 amount of carbonate phases observed in Syn-M and Com-M samples were not
480 as high due to the use of mortar samples, as well as the short curing age
481 investigated. Nevertheless, samples containing synthetic MgO still presented a
482 much higher amount of hydromagnesite in comparison to those with
483 commercial MgO (5.8% vs. 1.9%). Furthermore, a small amount of
484 nesquehonite (1.1%) was observed in Syn-M, although its peaks could not be
485 clearly detected in the XRD patterns due to their relatively low intensities.
486 Overall, the higher amount of total HMCs (6.9%) present in Syn-M samples as
487 opposed to Com-M samples (2.2%) could explain the higher strengths of the
488 former.

489

490 The increased formation of HMCs was facilitated by the higher reactivity of the
491 synthetic MgO (Fig. 5), which was also reflected by the increased utilization of
492 MgO. Accordingly, Syn-M samples revealed a low residual MgO content of
493 5.4%, whereas this value was as high as 76.5% in Com-M samples, highlighting
494 the presence of unreacted MgO. The higher utilization of MgO translated into
495 its increased dissolution and higher amounts of brucite precipitation in Syn-M
496 samples (79.5%) when compared to Com-M samples (13.7%). Therefore, the
497 use of synthetic MgO promoted both the hydration and subsequent carbonation
498 reactions by enabling the increased dissolution of MgO, which led to an
499 abundant formation of hydrate/carbonate phases. The low hydration rate of
500 Com-M samples could be related to their lower w/b ratio, as water provides the
501 medium for the hydration and carbonation of MgO grains. However, the
502 presence of water also reduces the diffusion of CO₂ within MgO-based concrete,
503 which may reduce the extent of carbonation [16, 34].

504

505 These differences in the reaction mechanisms of Syn-M and Com-M samples
506 reflected the potential of synthetic MgO in the development of MgO-based
507 samples with improved performance. Alternatively, the relatively high contents

508 of unhydrated MgO suggested a low hydration and carbonation rate in samples
509 involving the use of commercial MgO, which was associated with the low
510 reactivity of this binder, albeit being produced within a temperature range that
511 led to its classification as “reactive MgO”. These results highlight the potential
512 of these samples to gain even higher strengths via the optimization of the
513 production conditions of the initial binder component. The increased reactivity
514 of MgO not only enables its dissolution but also facilitates the higher formation
515 of hydrate/carbonate phases that lead to the densification of the microstructure
516 and increased strength gain [16, 60, 78].

517

518

519 **3.4 TGA/DSC**

520

521 The TGA/DSC results of Syn-M and Com-M samples after 7 days of curing are
522 displayed in Fig. 8. Three major decomposition stages, in line with the trends
523 reported in previous studies [79-85], were identified:

524

525 1. 50-320°C: Dehydration of water bonded to HMCs ($4\text{MgCO}_3 \cdot \text{Mg}(\text{OH})_2 \cdot 4\text{H}_2\text{O}$
526 $\rightarrow 4\text{MgCO}_3 \cdot \text{Mg}(\text{OH})_2 + 4\text{H}_2\text{O}$).

527

528 2. 320-480°C: Dehydroxylation of HMCs ($4\text{MgCO}_3 \cdot \text{Mg}(\text{OH})_2 \rightarrow 4\text{MgCO}_3 + \text{MgO}$
529 $+ \text{H}_2\text{O}$) and decomposition of uncarbonated brucite ($\text{Mg}(\text{OH})_2 \rightarrow \text{MgO} + \text{H}_2\text{O}$).

530

531 3. 480-900°C: Decarbonation of HMCs ($\text{MgCO}_3 \rightarrow \text{MgO} + \text{CO}_2$).

532

533 All the mass loss values associated with each of these stages is listed in Table
534 5. The decomposition trends revealed by the TGA/DSC results were in line with
535 the XRD quantification results (Table 4). Accordingly, the higher mass loss
536 revealed by Syn-M samples within all temperature ranges indicated the
537 increased reaction degrees within these samples in comparison to Com-M
538 samples. More specifically, the mass loss observed in Syn-M samples in the
539 320-480°C range (19.1%) in comparison to that of Com-M samples (7.4%)
540 revealed the higher hydration and carbonation of the former. The increased
541 hydration of Syn-M samples was also clearly revealed by the sharp peak at

542 ~380°C in the DSC curve, which had a much higher intensity than the
543 corresponding peak observed in Com-M samples. Similarly, the higher mass
544 loss in the 480-900°C range (2.9% vs. 1.7%) also reflected the enhanced
545 carbonation of Syn-M samples. Higher mass loss values could be expected if
546 samples were tested after longer (i.e. > 7 days) curing durations. Nevertheless,
547 the increased mass loss due to the enhanced hydration and carbonation of Syn-
548 M samples, associated with the higher reactivity of synthetic MgO as opposed
549 to commercial MgO, was in line with the XRD and strength results.

550

551

552 **3.5 Microstructure**

553

554 Fig. 9 shows the microstructural images of Syn-M and Com-M samples after 7
555 days of curing. The dominant phases observed in Com-M samples were
556 unreacted MgO and brucite, accompanied by the scarce formation of HMCs
557 (Figs. 10(a) and (b)). Alternatively, rosette-like hydromagnesite and needle-like
558 nesquehonite crystals were revealed in Syn-M samples (Figs. 9(d) and (e)) [86],
559 which were consistent with the XRD and TGA/DSC results. The formation of
560 HMCs contributes to mechanical performance by not only filling in the available
561 pores and thereby densifying the microstructure [16], but also forming a
562 compact and interlocked 3D network [87]. Accordingly, the denser
563 microstructures dominated by the widespread formation of carbonate crystals
564 within Syn-M samples could explain their higher mechanical performance than
565 Com-M samples, which revealed a more porous structure.

566

567 Another aspect that differentiated the two samples from each other was the
568 interface between the sand particles and cement paste. Considering that the
569 bonding between sand and cement paste within the transition zone is critical in
570 the determination of strength [88], the properties of this interface could also play
571 a key role in the performance of both samples. Accordingly, a very porous
572 interface dominated by unreacted MgO and brucite particles was observed in
573 Com-M samples (Fig. 9(c)), which was different from the surrounding bulk paste.
574 On the other hand, the interface observed in Syn-M samples (Figs. 9(e) and (f))
575 had a more compact structure incorporating various carbonate crystals. The

576 higher density of this interface was associated with the expansive formation of
577 HMCs [5], which filled the gap between the sand particles and surrounding
578 paste. Furthermore, the binding strength provided by the carbonate crystals
579 could have also contributed to the strength of the bond and adhesion between
580 the hydrated/carbonated paste and sand particles [89], explaining the improved
581 performance of Syn-M samples over Com-M samples.

582

583

584 **3.6 Carbon footprint**

585

586 Fig. 10 shows the total CO₂ emissions associated with the production of
587 synthetic MgO and commercial MgO [1]. These results clearly indicate the
588 higher amount of CO₂ emitted during the production of synthetic MgO, which
589 was ~62% higher than that of commercial MgO. The higher emissions were
590 mainly attributed to the production of the alkali source, NaOH, which was used
591 to enable the precipitation of Mg(OH)₂ from the brine solution. The production
592 of NaOH involves the use of electrolysis, which is an energy-intensive process,
593 resulting in a large carbon footprint that is ~3.5 times higher than the CO₂
594 emissions due to the calcination of brucite. Fig. 11 shows the outcome of the
595 sensitivity analysis in terms of the influence of energy type on CO₂ emissions
596 associated with the production of 1 kg of synthetic MgO, demonstrating the
597 importance of energy sources in determining the final outcome. Accordingly,
598 the use of nuclear power resulted in the lowest carbon emissions associated
599 with synthetic MgO production. Alternatively, the adoption of coal, which led to
600 1.6 times higher emissions than those observed under nuclear power, was not
601 favored in terms of the carbon footprint.

602

603 The overall CO₂ emissions of MgO production could be further reduced via the
604 identification of alternative alkali sources (e.g. CaO from the decomposition of
605 oyster shells [90]) with potentially lower environmental impacts that could be
606 used instead of NaOH during this process, which could also present a more
607 economical route. Alternative production routes for NaOH, which can be
608 manufactured on-site by the electrolysis of NaCl brine, as well as its recycling
609 would also reduce the total emissions of synthetic MgO [91]. Alternatively, the

610 production of NaOH from other sources such as solar salt could significantly
611 enable the reduction of environmental impacts associated with the production
612 of MgO via the wet route [92]. Another aspect to be considered when evaluating
613 the net CO₂ emissions of MgO-based binders is the amount of CO₂ that could
614 be absorbed during their use in concrete products. Theoretically, the complete
615 carbonation of 1 kg of MgO can enable the sequestration of ~1.1 kg CO₂ (based
616 on theoretical calculations), which could be feasible considering the high
617 reactivity of the MgO produced through the wet route (i.e. from reject brine) [1].
618 This could be further supported with the use of renewable energy sources that
619 would enable the reduction of overall CO₂ emissions associated with the
620 production of the synthetic MgO.

621

622

623 **4. Conclusions**

624

625 Reject brine, obtained as a by-product at the end of the desalination process,
626 presents a great potential for the production of MgO. This study investigated
627 the production, use and environmental impacts of MgO extracted from a locally-
628 obtained reject brine (via the wet route), and provided a comparison with a
629 commercial MgO produced via the calcination of magnesite (via the dry route).
630 As a cementitious binder, synthetic MgO extracted from reject brine
631 outperformed its commercial counterpart in terms of mechanical performance,
632 which was attributed to its higher reactivity. The high reactivity of synthetic MgO
633 led to enhanced hydration and carbonation reactions, resulting in the increased
634 formation of hydrate and carbonate phases such as hydromagnesite and
635 nesquehonite. In addition to the binding network established via the formation
636 of these carbonate phases, the dense sand-cement paste interface composed
637 of large carbonate crystals contributed to the improved performance of
638 synthetic MgO-based samples. Alternatively, the highly porous interfacial zone
639 observed in samples containing commercial MgO, which was attributed to the
640 low dissolution and utilization of MgO in hydration and carbonation reactions
641 due to its low reactivity, could explain its inferior performance.

642

643 The use of reject brine in the production of MgO has a high significance as the

644 local production of cement from locally available waste materials and by-
645 products can save natural resources and mitigate the current threat of
646 desalination to marine organisms. Furthermore, the use of the proposed
647 binders will pave the way for the sequestration of atmospheric CO₂ as stable
648 carbonates in cement-based mixes. One aspect that could be improved
649 regarding the production of MgO is the scaling up of the process to enable its
650 synthesis in an effective manner, which would lead to the reduction of the
651 environmental implications. During this process, the alkali source used to
652 enable the precipitation of the precursor, Mg(OH)₂, determines the overall
653 environmental impact of the production process. This is because the production
654 of the alkali base is often an energy-intensive process, making the largest
655 contribution to the environmental score. Identification of alkali sources that can
656 be produced through energy-efficient routes and are recyclable at the end of
657 this process, as well as the incorporation of alternative energy sources that rely
658 on renewable resources in the manufacturing process, will increase the
659 sustainability of the final product, resulting in high purity products with an
660 enhanced performance and low environmental impact.

661

662

663 **Acknowledgement**

664

665 The authors would like to thank Mr Fanxi Sun for his help with the experimental
666 work. The authors also acknowledge the financial support from the Singapore
667 MOE Academic Research Fund Tier 1 (RG 95/16) for the completion of this
668 research project.

Appendix

1. The heat absorption with respect to the decomposition of 1.45 kg of brucite at 500°C (773 K) (T=Temperature (k)/1000):

$$\Delta H_{\text{brucite}} = 84.90T + 74.4T^2/2 - 68.92T^3/3 + 26.63T^4/4 + 2.17/T - 960.04 + 924.66$$

$$= 4.70 \cdot 10^4 \text{ J/mol} = 810.3 \text{ J/g} = 1175 \text{ kJ}$$

$$\Delta H_{\text{MgO}} = 47.25T + 5.68T^2/2 - 0.872T^3/3 + 0.1T^4/4 + 1.05/T - 691.1 + 601.24$$

$$= 2.15 \cdot 10^4 \text{ J/mol} = 537 \text{ J/g} = 537.5 \text{ kJ}$$

$$\Delta H_{\text{H}_2\text{O}} = -203.6T + 1523.29T^2/2 - 3193.41T^3/3 + 2474.45T^4/4 - 3.85/T -$$

$$256.54 + 285.83 = 5.12 \cdot 10^4 \text{ J/mol} = 2844.4 \text{ J/g} = 1280 \text{ kJ}$$

$$Q_1 = 1280 \text{ kJ} + 537.5 \text{ kJ} - 1175 \text{ kJ} = 642.5 \text{ kJ}$$

2. The amount of heat needed to heat 0.45 kg of H₂O from 25°C (298 K) to 500°C (773 K) (T=Temperature (k)/1000)

$$Q_2 = \int_{298}^{773} c_p dt = \int_{298}^{773} (-203.6 + 1523.29 T - 3193.41 T^2 + 2474.45 T^3 + 3.855/T^2) dT$$

$$= 5.18 \cdot 10^4 \text{ J/mol} = 2877.7 \text{ J/g} = 1295.0 \text{ kJ}$$

3. The amount of heat needed to heat 1 kg of MgO from 25°C (298 K) to 500°C (773 K) (T=Temperature (k)/1000)

$$Q_3 = \int_{298}^{773} c_p dT = \int_{298}^{773} (47.25 + 5.68 T - 0.872 T^2 + 0.104 T^3 - 1.05/T^2) dT$$

$$= 2.15 \cdot 10^4 \text{ J/mol} = 537.5 \text{ J/g} = 537.5 \text{ kJ}$$

$$Q_{\text{total}} = Q_1 + Q_2 + Q_3 = 2475 \text{ kJ} = 0.687 \text{ kWh electricity}$$

References

- [1] S. Ruan, C. Unluer, Comparative life cycle assessment of reactive MgO and Portland cement production, *Journal of Cleaner Production* 137 (2016) 258-273.
- [2] S. Ruan, C. Unluer, Influence of supplementary cementitious materials on the performance and environmental impacts of reactive magnesia cement concrete, *Journal of Cleaner Production* 159 (2017) 62-73.
- [3] A. Fedoročková, M. Hreus, P. Raschman, G. Sučík, Dissolution of magnesium from calcined serpentinite in hydrochloric acid, *Minerals Engineering* 32 (2012) 1-4.
- [4] H. Dong, C. Unluer, E.-H. Yang, A. Al-Tabbaa, Synthesis of reactive MgO from reject brine via the addition of NH_4OH , *Hydrometallurgy* 169 (2017) 165-172.
- [5] M.A. Shand, *The chemistry and technology of magnesia*, John Wiley & Sons, 2006.
- [6] M.A. Caraballo, T.S. Rötting, F. Macías, J.M. Nieto, C. Ayora, Field multi-step limestone and MgO passive system to treat acid mine drainage with high metal concentrations, *Applied Geochemistry* 24(12) (2009) 2301-2311.
- [7] R.H. Dave, P.K. Ghosh, Enrichment of bromine in sea-bittern with recovery of other marine chemicals, *Industrial and Engineering Chemistry Research* 44(9) (2005) 2903-2907.
- [8] K.T. Tran, K.S. Han, S.J. Kim, M.J. Kim, T. Tran, Recovery of magnesium from Uyuni salar brine as hydrated magnesium carbonate, *Hydrometallurgy* 160 (2016) 106-114.
- [9] H. Dong, C. Unluer, E.-H. Yang, A. Al-Tabbaa, Recovery of reactive MgO from reject brine via the addition of NaOH, *Desalination* 429 (2018) 88-95.
- [10] H. Dong, C. Unluer, E.-H. Yang, F. Jin, A. Al-Tabbaa, Microstructure and carbon storage capacity of hydrated magnesium carbonates synthesized from different sources and conditions, *Journal of CO₂ Utilization* 34 (2019) 353-361.
- [11] F. Jin, A. Al-Tabbaa, Characterisation of different commercial reactive

- magnesia, *Advances in Cement Research* 26(2) (2014) 101-113.
- [12] E.-K. Lee, K.-D. Jung, O.-S. Joo, Y.-G. Shul, Magnesium oxide as an effective catalyst in catalytic wet oxidation of H₂S to sulfur, *Reaction Kinetics and Catalysis Letters* 82(2) (2004) 241-246.
- [13] L. Mo, M. Deng, M. Tang, A. Al-Tabbaa, MgO expansive cement and concrete in China: Past, present and future, *Cement and Concrete Research* 57 (2014) 1-12.
- [14] C. Unluer, A. Al-Tabbaa, Impact of hydrated magnesium carbonate additives on the carbonation of reactive MgO cements, *Cement and Concrete Research* 54 (2013) 87-97.
- [15] M. Liska, A. Al-Tabbaa, K. Carter, J. Fifield, Scaled-up commercial production of reactive magnesium cement pressed masonry units. Part I: Production, *Proceedings of the Institution of Civil Engineers-Construction Materials* 165(4) (2012) 211-223.
- [16] S. Ruan, C. Unluer, Influence of mix design on the carbonation, mechanical properties and microstructure of reactive MgO cement-based concrete, *Cement and Concrete Composites* 80 (2017) 104-114.
- [17] C. Sonat, N. Dung, C. Unluer, Performance and microstructural development of MgO–SiO₂ binders under different curing conditions, *Construction and Building Materials* 154 (2017) 945-955.
- [18] C. Sonat, C. Unluer, Development of magnesium-silicate-hydrate (MSH) cement with rice husk ash, *Journal of Cleaner Production* 211 (2019) 787-803.
- [19] G. Mármol, L. Mattoso, A.C. Correa, C.A. Fioroni, H. Savastano Jr, Influence of cellulose pulp on the hydration followed by fast carbonation of MgO-based binders, *Journal of CO₂ Utilization* 41 (2020) 101236.
- [20] R. Zhang, D.K. Panesar, Water absorption of carbonated reactive MgO concrete and its correlation with the pore structure, *Journal of CO₂ Utilization* 24 (2018) 350-360.
- [21] D. Zhao, Z. Wang, S. Lu, X. Shi, An amidoxime-functionalized polypropylene fiber: competitive removal of Cu (II), Pb (II) and Zn (II) from

wastewater and subsequent sequestration in cement mortar, *Journal of Cleaner Production* 274 (2020) 123049.

[22] Z. Tang, Z. Qiu, S. Lu, X. Shi, Functionalized layered double hydroxide applied to heavy metal ions absorption: A review, *Nanotechnology Reviews* 9(1) (2020) 800-819.

[23] Y. Li, T. Shi, J. Li, Effects of fly ash and quartz sand on water-resistance and salt-resistance of magnesium phosphate cement, *Construction and Building Materials* 105 (2016) 384-390.

[24] Y. Li, Y. Li, T. Shi, J. Li, Experimental study on mechanical properties and fracture toughness of magnesium phosphate cement, *Construction and Building Materials* 96 (2015) 346-352.

[25] D. Zhang, H. Wu, V.C. Li, B.R. Ellis, Autogenous healing of Engineered Cementitious Composites (ECC) based on MgO-fly ash binary system activated by carbonation curing, *Construction and Building Materials* 238 (2020) 117672.

[26] L. Wang, K. Iris, D.C. Tsang, K. Yu, S. Li, C.S. Poon, J.-G. Dai, Upcycling wood waste into fibre-reinforced magnesium phosphate cement particleboards, *Construction and Building Materials* 159 (2018) 54-63.

[27] L. Wang, L. Chen, B. Guo, D.C. Tsang, L. Huang, Y.S. Ok, V. Mechtcherine, Red mud-enhanced magnesium phosphate cement for remediation of Pb and As contaminated soil, *Journal of Hazardous Materials* 400 (2020) 123317.

[28] P. Gao, X. Lu, F. Geng, X. Li, J. Hou, H. Lin, N. Shi, Production of MgO-type expansive agent in dam concrete by use of industrial by-products, *Building and Environment* 43(4) (2008) 453-457.

[29] M. Liska, A. Al-Tabbaa, Performance of magnesia cements in pressed masonry units with natural aggregates: Production parameters optimisation, *Construction and Building Materials* 22(8) (2008) 1789-1797.

[30] M. Liska, A. Al-Tabbaa, Ultra-green construction: reactive magnesia masonry products, *Proceedings of ICE-Waste and Resource Management* 162(4) (2009) 185-196.

- [31] N. Dung, C. Unluer, Improving the performance of reactive MgO cement-based concrete mixes, *Construction and Building Materials* 126 (2016) 747-758.
- [32] N. Dung, C. Unluer, Influence of nucleation seeding on the performance of carbonated MgO formulations, *Cement and Concrete Composites* 83 (2017) 1-9.
- [33] N. Dung, C. Unluer, Sequestration of CO₂ in reactive MgO cement-based mixes with enhanced hydration mechanisms, *Construction and Building Materials* 143 (2017) 71-82.
- [34] C. Unluer, A. Al-Tabbaa, Enhancing the carbonation of MgO cement porous blocks through improved curing conditions, *Cement and Concrete Research* 59 (2014) 55-65.
- [35] J. An, X. Xue, Life-cycle carbon footprint analysis of magnesia products, *Resources, Conservation and Recycling* 119 (2017) 4-11.
- [36] J. An, Y. Li, R.S. Middleton, Reducing energy consumption and carbon emissions of magnesia refractory products: a life-cycle perspective, *Journal of Cleaner Production* 182 (2018) 363-371.
- [37] H.-L. Wu, D. Zhang, B.R. Ellis, V.C. Li, Development of reactive MgO-based Engineered Cementitious Composite (ECC) through accelerated carbonation curing, *Construction and Building Materials* 191 (2018) 23-31.
- [38] D. Hassan, Environmental sustainability assessment and associated experimental investigations of magnesia production routes, University of Cambridge, 2014.
- [39] J. Li, Y. Zhang, S. Shao, S. Zhang, Comparative life cycle assessment of conventional and new fused magnesia production, *Journal of Cleaner Production* 91 (2015) 170-179.
- [40] X. Cong, S. Lu, Y. Yao, Z. Wang, Fabrication and characterization of self-ignition coal gangue autoclaved aerated concrete, *Materials and Design* 97 (2016) 155-162.
- [41] J. Li, Y. Zhang, S. Shao, S. Zhang, S. Ma, Application of cleaner production in a Chinese magnesia refractory material plant, *Journal of Cleaner Production*

113 (2016) 1015-1023.

[42] L.F. Greenlee, D.F. Lawler, B.D. Freeman, B. Marrot, P. Moulin, Reverse osmosis desalination: water sources, technology, and today's challenges, *Water Research* 43(9) (2009) 2317-2348.

[43] E. Jones, M. Qadir, M.T. van Vliet, V. Smakhtin, S.-m. Kang, The state of desalination and brine production: A global outlook, *Science of the Total Environment* 657 (2019) 1343-1356.

[44] PUB, Desalinated Water. Singapore's National Water Agency. <https://www.pub.gov.sg/watersupply/fournationaltaps/desalinatedwater>.

[45] M.H. El-Naas, Reject brine management, *Desalination, trends and technologies*, Croatia: InTech, 2011, pp. 237-252.

[46] A. Mohamed, M. Maraqa, J. Al Handhaly, Impact of land disposal of reject brine from desalination plants on soil and groundwater, *Desalination* 182(1-3) (2005) 411-433.

[47] H. Dong, E.-H. Yang, C. Unluer, F. Jin, A. Al-Tabbaa, Investigation of the properties of MgO recovered from reject brine obtained from desalination plants, *Journal of Cleaner Production* (2018).

[48] M.H. El-Naas, A.H. Al-Marzouqi, O. Chaalal, A combined approach for the management of desalination reject brine and capture of CO₂, *Desalination* 251(1-3) (2010) 70-74.

[49] R. Hao, Investigation into the production of carbonates and oxides from synthetic brine through carbon sequestration, Department of Engineering, University of Cambridge, 2017.

[50] D.H. Kim, A review of desalting process techniques and economic analysis of the recovery of salts from retentates, *Desalination* 270(1-3) (2011) 1-8.

[51] M. Turek, W. Gnot, Precipitation of magnesium hydroxide from brine, *Industrial and Engineering Chemistry Research* 34(1) (1995) 244-250.

[52] S. Ma, A.H. Akca, D. Esposito, S. Kawashima, Influence of aqueous carbonate species on hydration and carbonation of reactive MgO cement, *Journal of CO₂ Utilization* 41 (2020) 101260.

- [53] C. Fritzmann, J. Löwenberg, T. Wintgens, T. Melin, State-of-the-art of reverse osmosis desalination, *Desalination* 216(1-3) (2007) 1-76.
- [54] Y. Soong, A. Goodman, J. McCarthy-Jones, J. Baltrus, Experimental and simulation studies on mineral trapping of CO₂ with brine, *Energy Conversion and Management* 45(11-12) (2004) 1845-1859.
- [55] Y. Liu, M. Jia, C. Song, S. Lu, H. Wang, G. Zhang, Y. Yang, Enhancing ultra-early strength of sulphoaluminate cement-based materials by incorporating graphene oxide, *Nanotechnology Reviews* 9(1) (2020) 17-27.
- [56] Y. Liu, K. Yu, S. Lu, C. Wang, X. Li, Y. Yang, Experimental research on an environment-friendly form-stable phase change material incorporating modified rice husk ash for thermal energy storage, *Journal of Energy Storage* 31 (2020) 101599.
- [57] M.L. Druckenmiller, M.M. Maroto-Valer, Carbon sequestration using brine of adjusted pH to form mineral carbonates, *Fuel Processing Technology* 86(14-15) (2005) 1599-1614.
- [58] S. Casas, C. Aladjem, E. Larrotcha, O. Gibert, C. Valderrama, J.L. Cortina, Valorisation of Ca and Mg by-products from mining and seawater desalination brines for water treatment applications, *Journal of Chemical Technology and Biotechnology* 89(6) (2014) 872-883.
- [59] S. Ruan, J. Qiu, E.-H. Yang, C. Unluer, Fiber-reinforced reactive magnesia-based tensile strain-hardening composites, *Cement and Concrete Composites* 89 (2018) 52-61.
- [60] S. Ruan, C. Unluer, Effect of air entrainment on the performance of reactive MgO and PC mixes, *Construction and Building Materials* 142 (2017) 221-232.
- [61] C. Unluer, Carbon dioxide sequestration in magnesium-based binders, *Carbon Dioxide Sequestration in Cementitious Construction Materials*, Elsevier, 2018, pp. 129-173.
- [62] M. Muthu, S. Kumar, E.-H. Yang, C. Unluer, Degradation of carbonated reactive MgO-based concrete exposed to nitric acid, *Journal of CO₂ Utilization* 36 (2020) 210-219.

- [63] R. Zhang, D.K. Panesar, Design of carbonated r-MgO-PC binder system: Effect of r-MgO replacement level and water-to-binder ratio, *Journal of the American Ceramic Society* 103(1) (2020) 656-669.
- [64] R. Zhang, N. Bassim, D.K. Panesar, Characterization of Mg components in reactive MgO–Portland cement blends during hydration and carbonation, *Journal of CO₂ Utilization* 27 (2018) 518-527.
- [65] L. Vandeperre, M. Liska, A. Al-Tabbaa, Microstructures of reactive magnesia cement blends, *Cement and Concrete Composites* 30(8) (2008) 706-714.
- [66] PUB, Desalinated Water, <https://www.pub.gov.sg/watersupply/fournationaltaps/desalinatedwater> (2019).
- [67] ASTM, C109 / C109M-16a Standard Test Method for Compressive Strength of Hydraulic Cement Mortars (Using 2-in, or [50-mm] Cube Specimens), ASTM International, West Conshohocken, PA, United States, 2016.
- [68] L. Pu, C. Unluer, Investigation of carbonation depth and its influence on the performance and microstructure of MgO cement and PC mixes, *Construction and Building Materials* 120 (2016) 349-363.
- [69] R.W. Cheary, A. Coelho, A fundamental parameters approach to X-ray line-profile fitting, *Journal of Applied Crystallography* 25(2) (1992) 109-121.
- [70] R.K. Pachauri, A. Reisinger, IPCC fourth assessment report, IPCC, Geneva 2007 (2007).
- [71] ETH-ESU, Ökoinventare von Energiesystemen. ESU Group, ETH Technical University of Zürich, (1996).
- [72] M.W. Chase, Jr., NIST-JANAF Thermochemical Tables, Fourth Edition, *Journal of Physical and Chemical Reference Data. Monograph 9* (1998) 1-1951.
- [73] U.S. Energy Information Administration. <https://www.eia.gov/international/analysis/country/SGP>, (2016).
- [74] H. Dong, E.-H. Yang, C. Unluer, F. Jin, A. Al-Tabbaa, Investigation of the

properties of MgO recovered from reject brine obtained from desalination plants, *Journal of Cleaner Production* 196 (2018) 100-108.

[75] V. Moorthy, G. Kamat, Influence of origin and calcination treatments on the physical properties of magnesia powders, *Transactions of the Indian Ceramic Society* 28(1) (1969) 1-8.

[76] F. Harper, Effect of calcination temperature on the properties of magnesium oxides for use in magnesium oxychloride cements, *Journal of Chemical Technology and Biotechnology* 17(1) (1967) 5-10.

[77] C. Unluer, Enhancing the carbonation of reactive magnesia cement-based porous blocks, University of Cambridge, 2012.

[78] S. Ruan, J. Liu, E.-H. Yang, C. Unluer, Performance and microstructure of calcined dolomite and reactive magnesia-based concrete samples, *Journal of Materials in Civil Engineering* 29(12) (2017) 04017236.

[79] V. Vágvölgyi, R.L. Frost, M. Hales, A. Locke, J. Kristóf, E. Horváth, Controlled rate thermal analysis of hydromagnesite, *Journal of Thermal Analysis and Calorimetry* 92(3) (2008) 893-897.

[80] L.A. Hollingbery, T.R. Hull, The thermal decomposition of huntite and hydromagnesite—A review, *Thermochimica Acta* 509(1–2) (2010) 1-11.

[81] G. Jauffret, J. Morrison, F. Glasser, On the thermal decomposition of nesquehonite, *Journal of Thermal Analysis and Calorimetry* 122(2) (2015) 601-609.

[82] R.L. Frost, S. Bahfenne, J. Graham, W.N. Martens, Thermal stability of artinite, dypingite and brugnatellite—implications for the geosequestration of green house gases, *Thermochimica Acta* 475(1-2) (2008) 39-43.

[83] R.L. Frost, S.J. Palmer, Infrared and infrared emission spectroscopy of nesquehonite $\text{Mg}(\text{OH})(\text{HCO}_3)\cdot 2\text{H}_2\text{O}$ —implications for the formula of nesquehonite, *Spectrochimica Acta Part A: Molecular and Biomolecular Spectroscopy* 78(4) (2011) 1255-1260.

[84] S. Purwajanti, L. Zhou, Y. Ahmad Nor, J. Zhang, H. Zhang, X. Huang, C. Yu, Synthesis of magnesium oxide hierarchical microspheres: a dual-functional

material for water remediation, *ACS Applied Materials and Interfaces* 7(38) (2015) 21278-21286.

[85] P. Ballirano, C. De Vito, V. Ferrini, S. Mignardi, The thermal behaviour and structural stability of nesquehonite, $\text{MgCO}_3 \cdot 3\text{H}_2\text{O}$, evaluated by in situ laboratory parallel-beam X-ray powder diffraction: new constraints on CO_2 sequestration within minerals, *Journal of Hazardous Materials* 178(1) (2010) 522-528.

[86] P.J. Davies, B. Bubela, The transformation of nesquehonite into hydromagnesite, *Chemical Geology* 12(4) (1973) 289-300.

[87] P. De Silva, L. Bucea, D.R. Moorehead, V. Sirivivatnanon, Carbonates binders: reaction kinetics, strength and microstructure, *Cement and Concrete Composites* 28 (2006) 613–620.

[88] A.M. Brandt, *Cement-based composites: materials, mechanical properties and performance*, CRC Press, 2005.

[89] P. De Silva, L. Bucea, V. Sirivivatnanon, Chemical, microstructural and strength development of calcium and magnesium carbonate binders, *Cement and Concrete Research* 39(5) (2009) 460-465.

[90] The electrolytic extraction of magnesium from seawater. <http://what-when-how.com/materialsparts-and-finishes/magnesium-and-alloys/>.

[91] T.A. Davis, *Zero Discharge Seawater Desalination: Integrating the Production of Freshwater, Salt, Magnesium, and Bromine*. Desalination and Water Purification Research Development Program Report No. 111, 2007.

[92] D.A. Salas, A.D. Ramirez, N. Ulloa, H. Baykara, A.J. Boero, Life cycle assessment of geopolymer concrete, *Construction and Building Materials* 190 (2018) 170-177.

List of Tables:

Table 1 Composition of the reject brine used in this study, obtained by ICP-OES.

Element	Na	Mg	Ca	K	Si	B	Sr	Li	P and Al
Concentration (PPM)	16580	1603	484	998	0.15	4.31	19.6	0.92	< 0.2

Table 2 Chemical composition of commercial reactive MgO.

Constituent	MgO	SiO ₂	CaO	K ₂ O	Na ₂ O	Al ₂ O ₃	Fe ₂ O ₃
Chemical composition (%)	97	1.3	1.3	-	-	0.2	0.2

Table 3 Mix compositions prepared with different MgO sources.

Mix	Synthetic MgO	Commercial MgO	s/b ratio	w/b ratio
Syn-M	100%	0	1	0.83
Com-M	0	100%	1	0.53

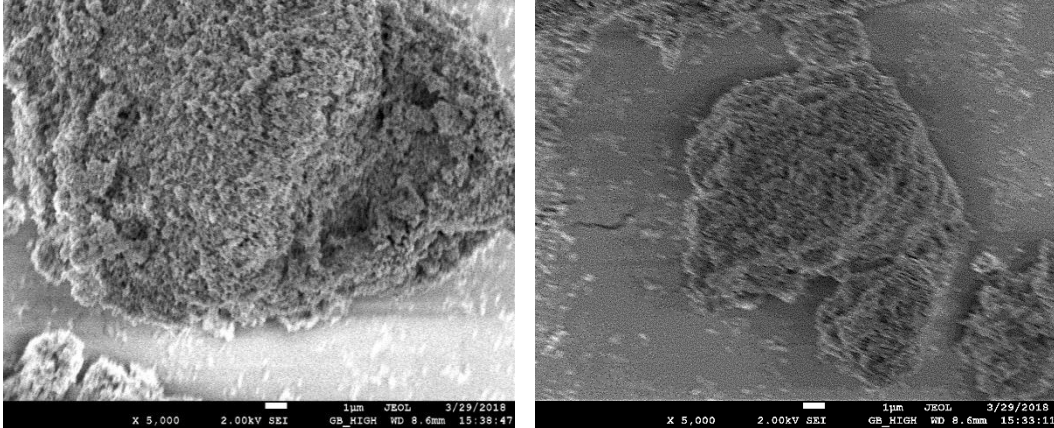
Table 4 Quantification of major phases within samples after 7 days of curing, calculated by XRD Rietveld analysis.

Mix	MgO (%)	Brucite (%)	Quartz (%)	Hydromagnesite (%)	Nesquehonite (%)	Total HMCs (%)
Syn-M	5.4	79.5	8.2	5.8	1.1	6.9
Com-M	76.5	13.7	7.6	1.9	0.3	2.2

Table 5 Mass loss of samples after 7 days of curing, obtained by TGA.

Mix	Mass loss (%)			
	50-320°C	320-480°C	480-900°C	Total
Syn-M	5.8	19.1	2.9	27.8
Com-M	3.3	7.4	1.7	12.4

List of Figures:



(a)

(b)

Fig. 1 Microstructural images of (a) MgO synthesized from reject brine and (b) commercially obtained MgO

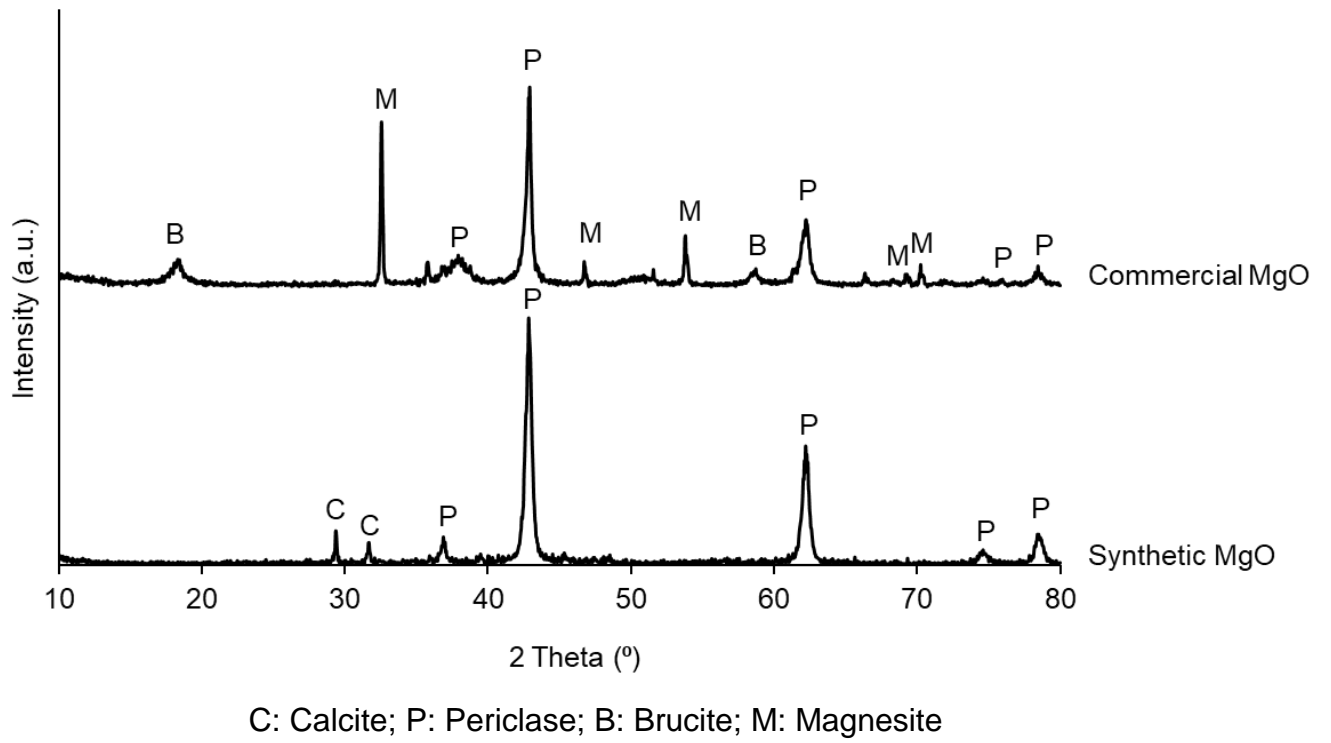


Fig. 2 XRD patterns of synthetic MgO and commercial MgO

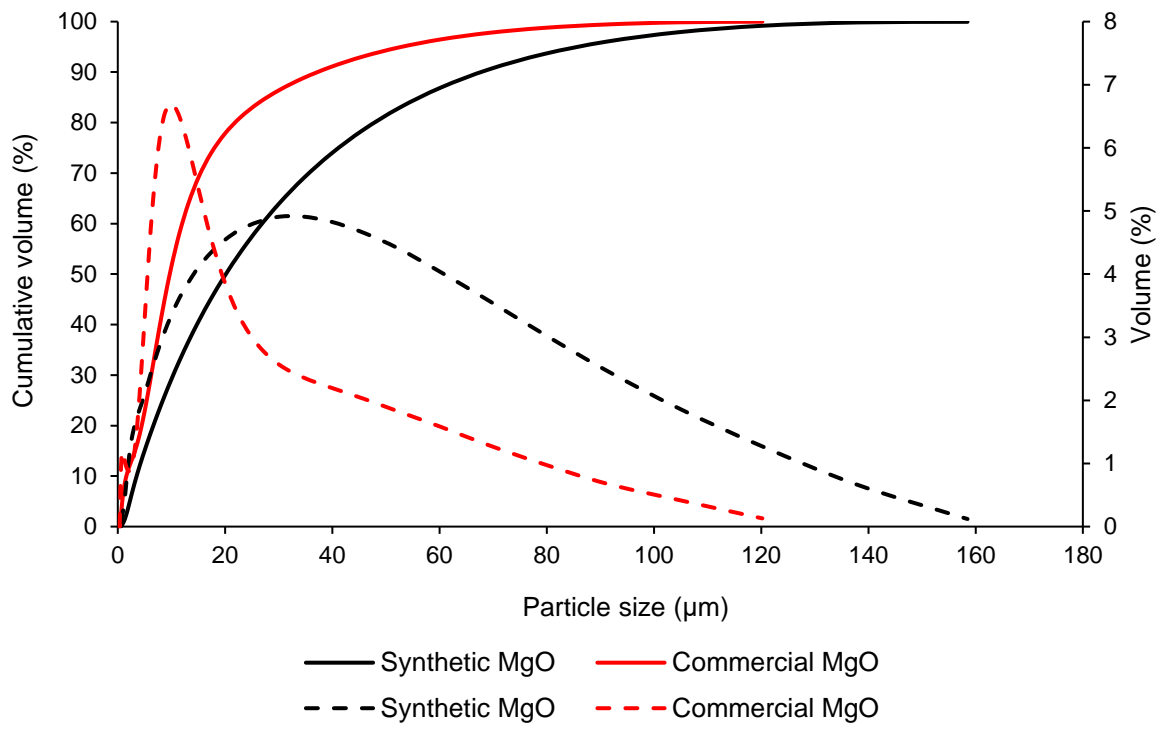


Fig. 3 Particle size distribution (PSD) of synthetic MgO and commercial MgO

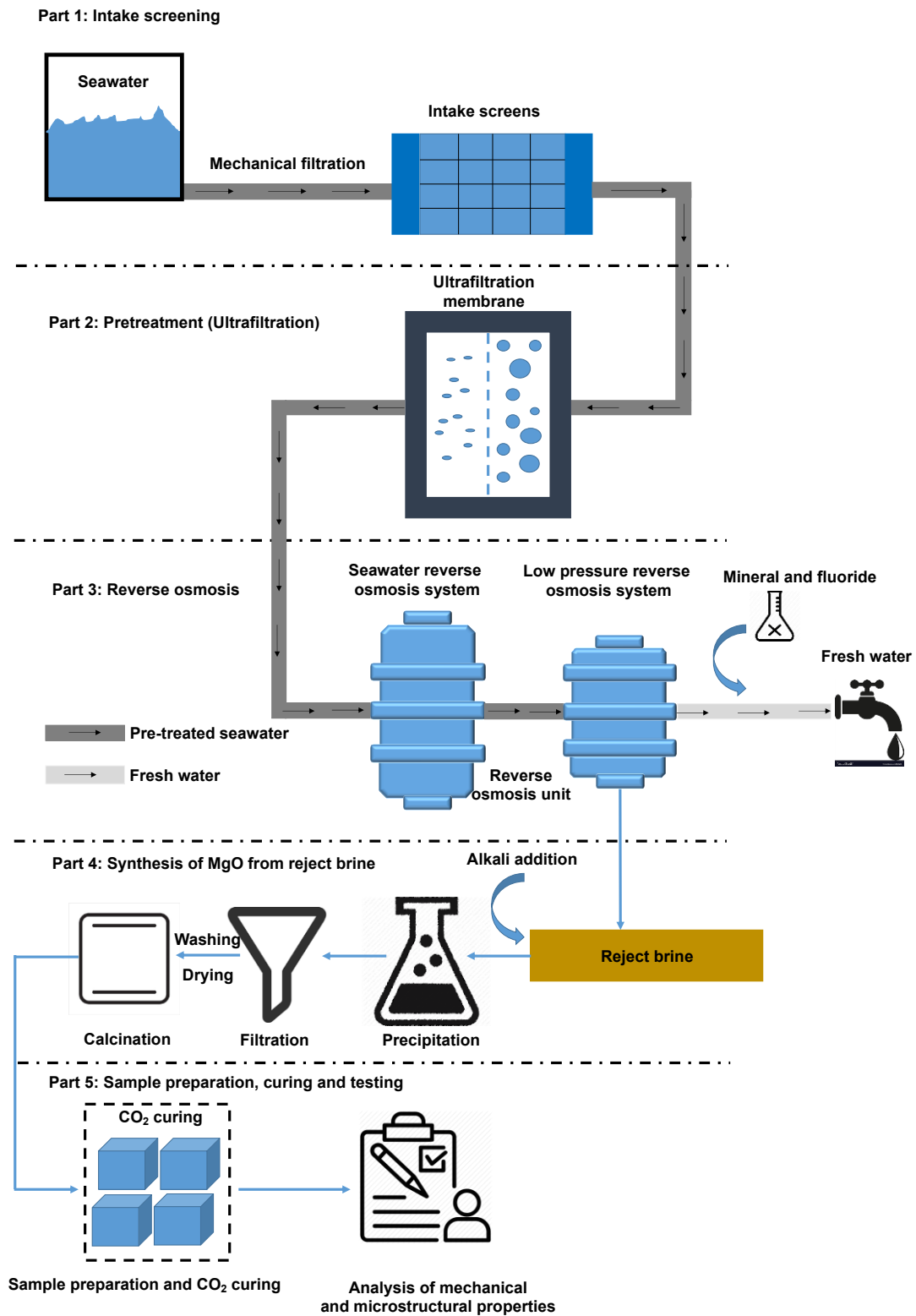


Fig. 4 Summary of the procedure starting with the acquirement of reject brine from a desalination plant to the synthesis and use of MgO in the preparation and analysis of samples

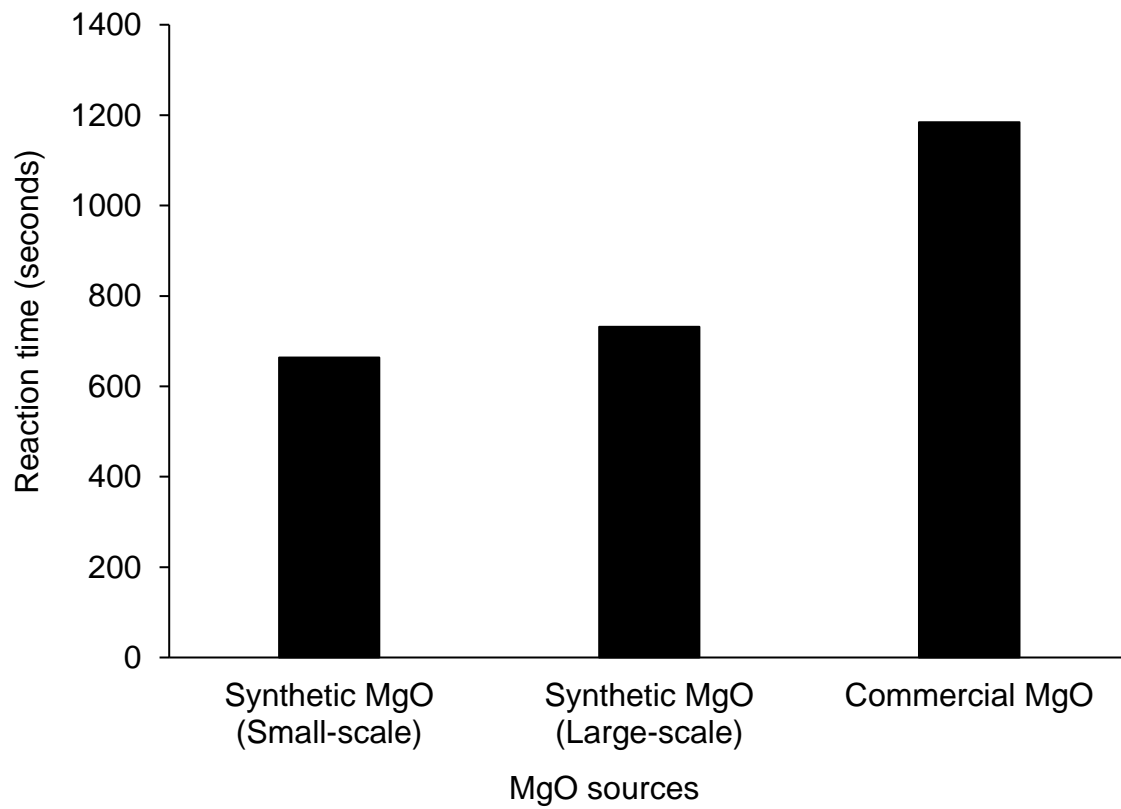


Fig. 5 Reactivity of synthetic MgO (i.e. produced from small- and large-scale lab trials) and commercial MgO

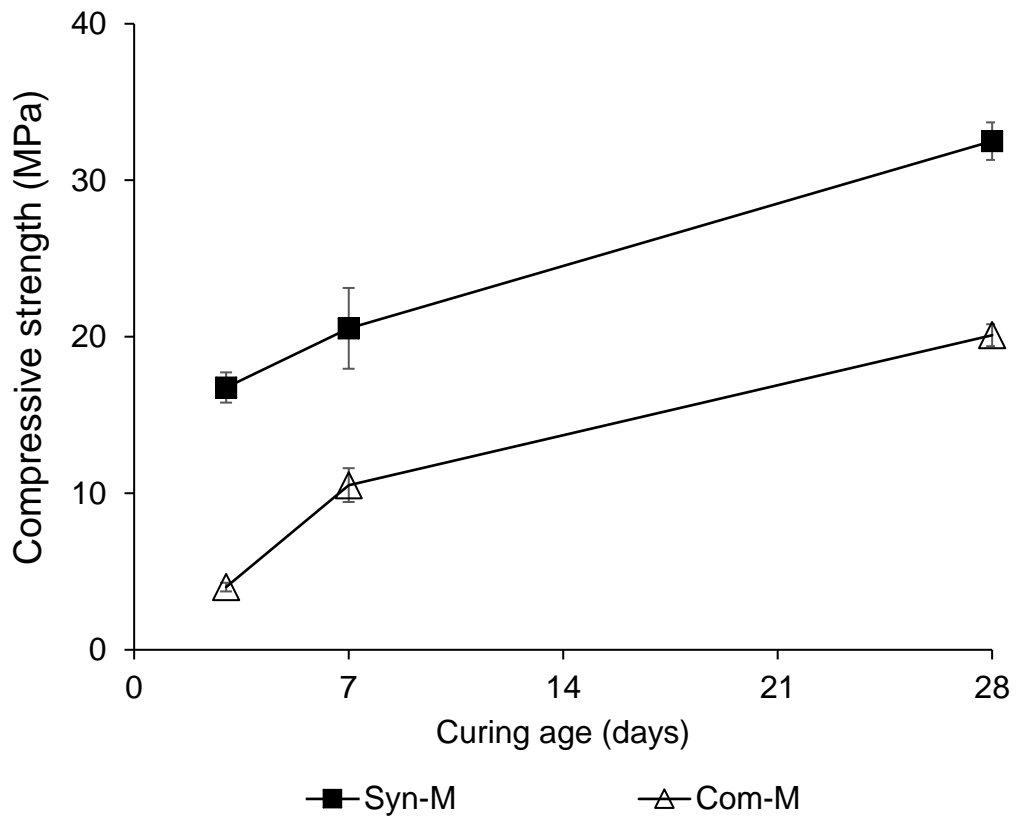


Fig. 6 Compressive strength of the synthetic and commercial MgO-based samples cured for up to 28 days

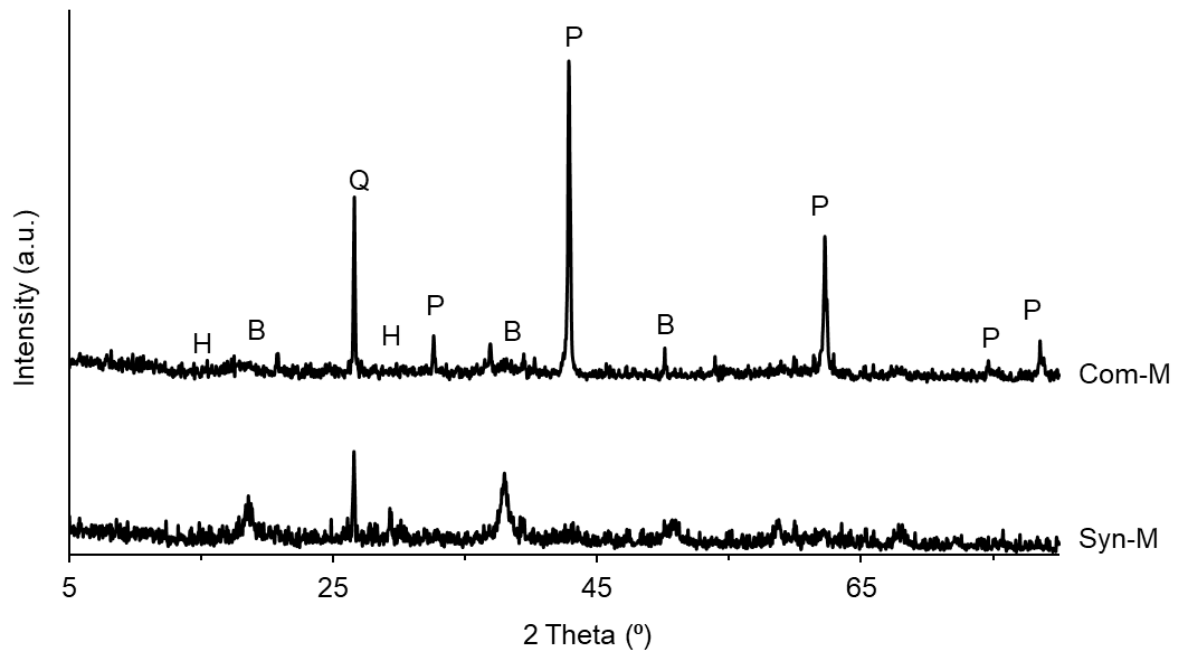


Fig. 7 XRD patterns of synthetic and commercial MgO-based samples after 7 days of curing (P: Periclase; B: Brucite; H: Hydromagnesite Q: Quartz)

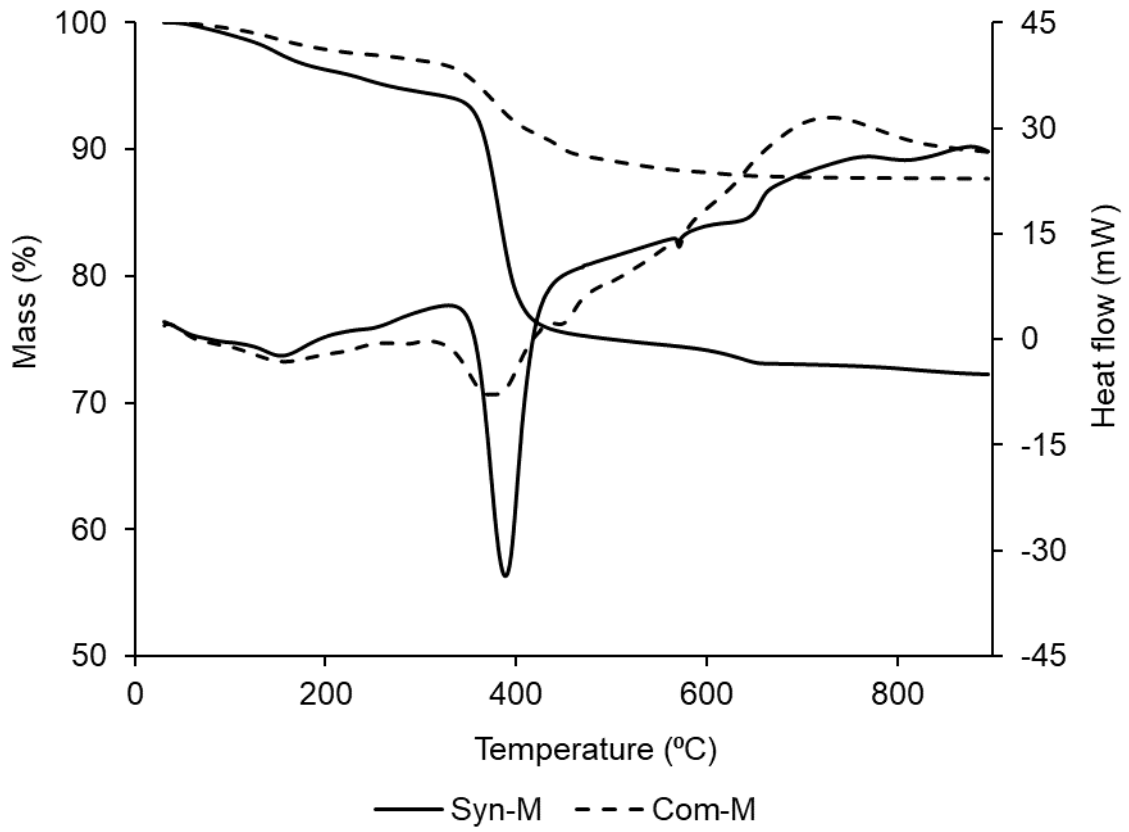
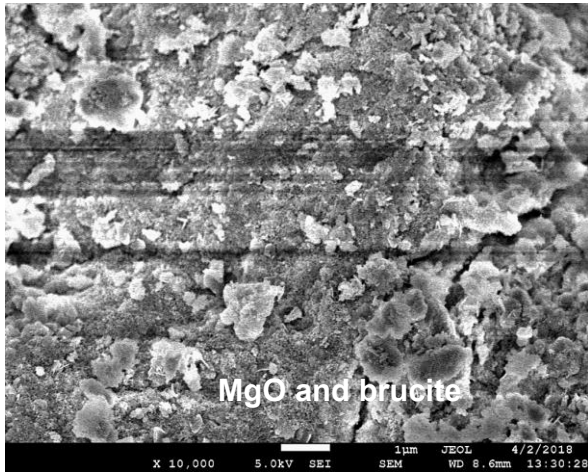


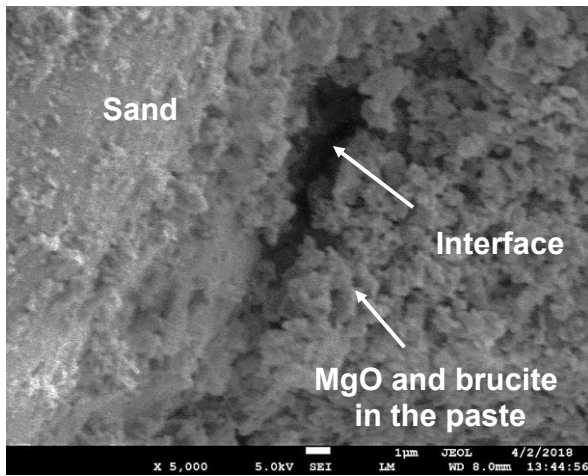
Fig. 8 TG/DSC curves of synthetic and commercial MgO-based samples after 7 days of curing



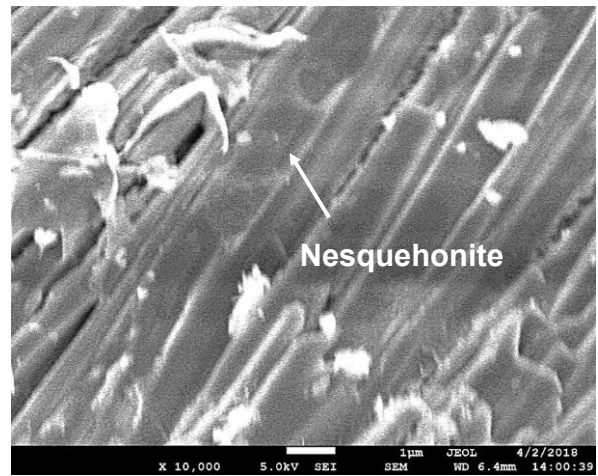
(a)



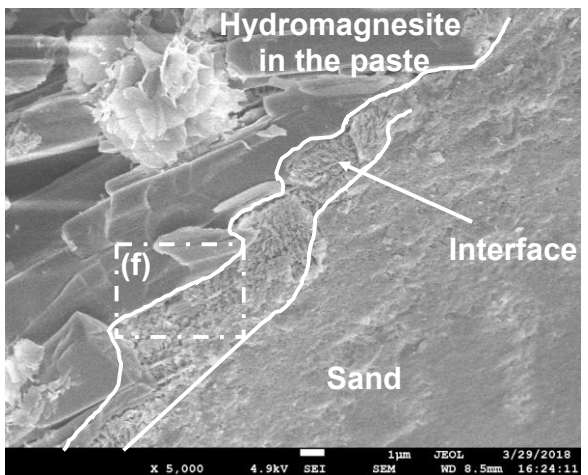
(b)



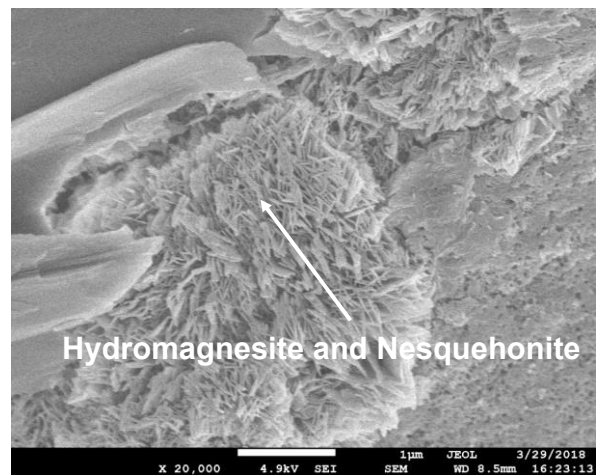
(c)



(d)



(e)



(f)

Fig. 9 Microstructural images of (a)-(c) Com-M and (d)-(f) Syn-M samples after 7 days of curing

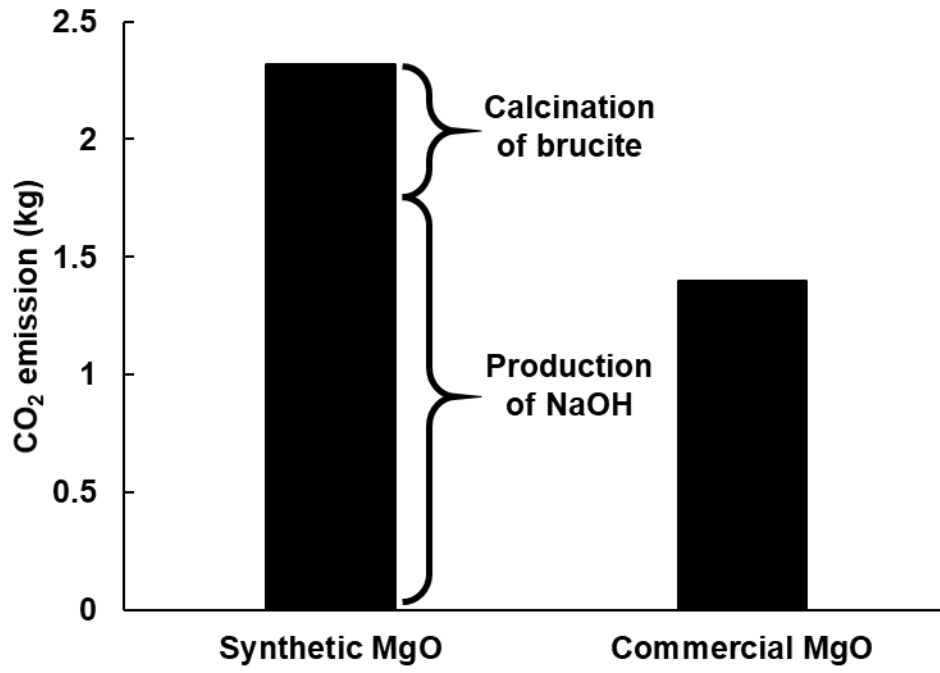


Fig. 10 CO₂ emissions associated with the production of 1kg of synthetic MgO and commercial MgO

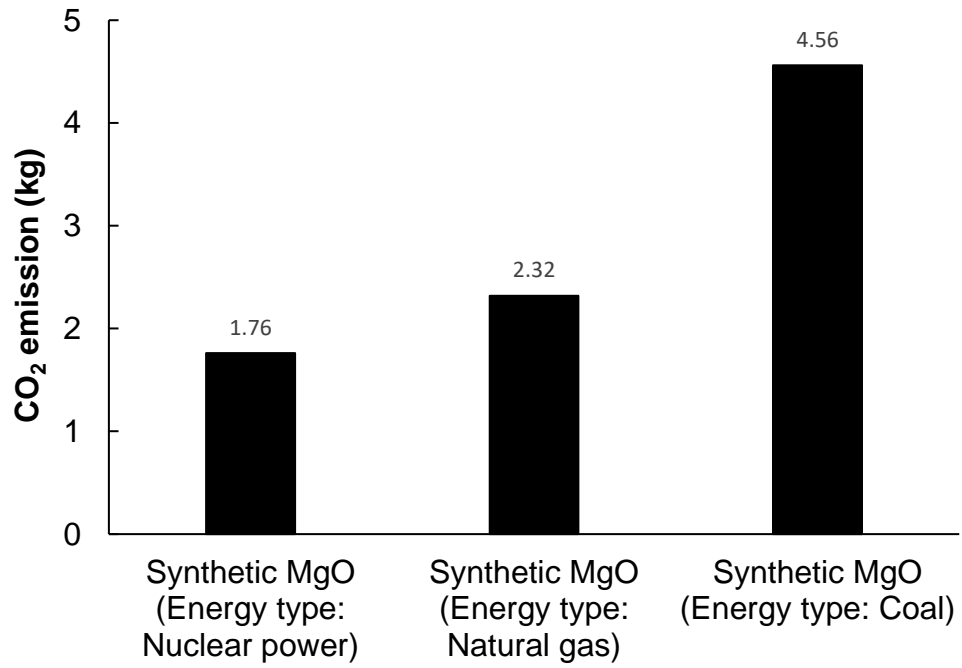


Fig. 11 Results of the sensitivity analysis showing the influence of the energy type on the CO₂ emissions associated with the production of 1 kg of synthetic MgO